Improvement of Surface Longwave Flux Algorithms Used in CERES Processing

SHASHI K. GUPTA

Science Systems and Applications, Inc., Hampton, Virginia

DAVID P. KRATZ AND PAUL W. STACKHOUSE JR.

NASA Langley Research Center, Hampton, Virginia

ANNE C. WILBER, TAIPING ZHANG, AND VICTOR E. SOTHCOTT

Science Systems and Applications, Inc., Hampton, Virginia

(Manuscript received 28 December 2009, in final form 8 March 2010)

ABSTRACT

An improvement was developed and tested for surface longwave flux algorithms used in the Clouds and the Earth's Radiant Energy System processing based on lessons learned during the validation of global results of those algorithms. The algorithms involved showed significant overestimation of downward longwave flux for certain regions, especially dry–arid regions during hot times of the day. The primary cause of this overestimation was identified and the algorithms were modified to (i) detect meteorological conditions that would produce an overestimation, and (ii) apply a correction when the overestimation occurred. The application of this correction largely eliminated the positive bias that was observed in earlier validation studies. Comparisons of validation results before and after the application of correction are presented.

1. Introduction

The Clouds and the Earth's Radiant Energy System (CERES) project is an investigation of cloud–radiation interactions in the earth's climate system (Wielicki et al. 1996). To date, one CERES instrument has been flown on the Tropical Rainfall Measuring Mission (TRMM) satellite launched in November 1997, and two each on *Terra* and *Aqua* satellites launched respectively in December 1999 and May 2002. These instruments carry radiometers for making top-of-atmosphere (TOA) measurements of reflected and earth-emitted radiation in three broadband channels: a shortwave (SW) channel (0.2–5.0 μm), a total channel (from 0.2 to >100 μm), and a thermal infrared (IR) window channel (8–12 μm). An extensive modeling effort is subsequently used with TOA measurements for deriving surface SW and longwave (LW) fluxes and corresponding flux profiles at multiple levels in the atmosphere.

The three LW algorithms discussed in this study are part of the surface-only flux algorithms (SOFA) segment of the modeling effort within CERES inversion processing (Loeb et al. 2005, 2007). These algorithms are based on TOA-to-surface transfer methods or fast radiation parameterizations and are designated LW Models A, B, and C respectively. Two of these algorithms [Model A (Inamdar and Ramanathan 1997) and Model B (Gupta et al. 1992)] have been used in CERES processing to date (editions1 and 2) and are discussed in detail in Kratz et al. (2010). The third one (Model C; Zhou et al. 2007) has been tested recently and is being introduced for the next round (edition 3) of reprocessing. All algorithms make use of CERES TOA measurements, products derived from those measurements, and the ancillary meteorological database used for all CERES processing known as Meteorology, Ozone, and Aerosols (MOA). The use of the above inputs in these algorithms differs significantly because of differences between basic assumptions of each algorithm. A brief description of the models and input data is presented in section 2. A description of the flux overestimation problem over dry/arid regions in all of the above algorithms is presented in section 3. The methodology for remedying this overestimation is presented in

Corresponding author address: Dr. Shashi K. Gupta, Science Systems and Applications, Inc., Suite 200, One Enterprise Parkway, Hampton, VA 23666.
E-mail: shashi.k.gupta@nasa.gov

DOI: 10.1175/2010JAMC2463.1

section 4. Results from the application of methodology, including comparisons of new and old results, are shown in section 5, followed by concluding remarks in section 6.

2. Models and input data

a. LW Model A

This algorithm was developed by Inamdar and Ramanathan (1997) and is based on the premise that downward LW flux (DLF) at the surface is substantially correlated with outgoing LW radiation (OLR) at the TOA through the OLR component in the window (8–12 μm) region. The correlation was developed in terms of OLR components inside and outside the window region, hereafter referred to as window and nonwindow components respectively. Broadband (bb) DLF denoted as F_{Abb} was derived as

$$F_{\mathrm{Abb}} = F_{\mathrm{Awn}} + F_{\mathrm{Anw}}, \tag{1}$$

where the terms on the right-hand side represent window (wn) and nonwindow (nw) components respectively, and "A" in the subscript signifies Model A. Computations in this model are done in terms of fluxes normalized with surface blackbody emission (σT_s^4, where σ is the Stefan–Boltzmann constant and T_s is the surface temperature). Hence, Eq. (1) may be rewritten as

$$f_{\mathrm{Abb}} = f_{\mathrm{Awn}} + f_{\mathrm{Anw}}, \tag{2}$$

where $f_{\mathrm{Abb}} = F_{\mathrm{Abb}}/\sigma T_s^4$, and components f_{Awn} and f_{Anw} are similarly normalized. These components were derived separately using complex equations of the form

$$f_{\mathrm{Awn}} = g_1(w, T_s, T_a, u_{\mathrm{Swn}}, u_{\mathrm{Twn}}), \tag{3}$$

and

$$f_{\mathrm{Anw}} = g_2(w, T_s, T_a, u_{\mathrm{Snw}}, u_{\mathrm{Tnw}}), \tag{4}$$

where w is the column water vapor, T_s is the surface (skin) temperature, T_a is the air temperature 50 hPa above the surface, and u_{Swn}, u_{Twn}, u_{Snw}, and u_{Tnw} are surface and TOA upward fluxes in window and nonwindow regions respectively, also normalized the same way as f_{Abb}. The explicit forms of those equations are too complex to be reproduced here and the reader is referred to the original paper cited previously for details of the algorithm (see also Kratz et al. 2010). Finally, corresponding flux components were obtained by multiplying f_{Awn} and f_{Anw} by σT_s^4. Also, since the correlation between OLR and DLF essentially breaks down in the presence of clouds (Stephens and Webster 1984), this model works only for clear-sky conditions.

b. LW Model B

The current version of this algorithm was presented by Gupta et al. (1992; see also Gupta 1989) and is based on the premise that OLR and DLF are largely decoupled not only in the presence of clouds but also for clear skies, especially on smaller spatial and temporal scales (Stephens and Webster 1984; Stephens et al. 1994). Clear-sky DLF in this algorithm, denoted as F_{Bclr}, is derived using a parameterized radiation model and atmospheric state variables as

$$F_{\mathrm{Bclr}} = g_3(w) T_e^{3.7}, \tag{5}$$

where $g_3(w)$ is a function of column water vapor as described in previously cited references and "B" in the subscript signifies Model B; T_e is the effective emitting temperature of the lower atmosphere derived as

$$T_e = 0.60 T_s + 0.35 T_1 + 0.05 T_2, \tag{6}$$

where T_s is the surface skin temperature, T_1 is the mean temperature of the surface to 800-hPa layer, and T_2 is the same for the 800–680-hPa layer. The layer definitions used above are related to the temperature profiles available from satellite sounders at the time of model development, and the weights used in Eq. (6) are based on recognition of the fact that the bulk of the clear-sky DLF reaching the surface originated very close to the surface (Gupta 1989). All-sky DLF (F_{Ball}) is derived as

$$F_{\mathrm{Ball}} = F_{\mathrm{Bclr}} + F_{\mathrm{Bcre}}, \tag{7}$$

where F_{Bcre} is the component related to the cloud radiative effect derived in this model as

$$F_{\mathrm{Bcre}} = g_4(T_{\mathrm{cb}}, w_c) A_c, \tag{8}$$

where T_{cb} is the cloud-base temperature, w_c is the column water vapor below the cloud base, g_4 is a function of the two, and A_c is the cloud fraction. For explicit forms of functions g_3 and g_4, the reader is referred to the previously cited references.

c. LW Model C

The current version of this model presented in Zhou et al. (2007; see also Zhou and Cess 2001) expresses DLF for the clear part of the scene (F_{Cclr}) as

$$F_{\mathrm{Cclr}} = g_5(T_s, w), \tag{9}$$

TABLE 1. List of sites providing ground-based measurements for comparison with model-derived fluxes. Sites used as examples of dry–arid regions are marked with asterisks.

Site	Lat (°N)	Lon (°E)	Network
South Pole	−90.0	0.0	GMD
Georg von Neumayer, Antarctica	−70.7	351.8	BSRN
Syowa	−69.0	39.6	BSRN
Lauder, New Zealand	−45.0	169.7	BSRN
De Aar, South Africa*	−30.7	24.0	BSRN
Florianopolis, Brazil	−27.5	311.5	BSRN
Alice Springs, Australia*	−23.8	133.9	BSRN
American Samoa	−14.2	189.4	GMD
Manus	−2.1	147.4	ARM
Nauru	−0.5	166.9	ARM
Kwajalein	8.8	167.7	GMD
Tamanrasset, Algeria*	22.8	5.5	BSRN
Solar Village, Saudi Arabia*	24.9	46.4	BSRN
Sede Boqer, Israel*	30.9	34.8	BSRN
Bermuda	32.3	295.2	GMD
Goodwin Creek, MS	34.3	270.1	SURFRAD
Tateno, Japan	36.1	140.1	BSRN
ARM/Southern Great Plains, OK	36.6	262.5	ARM
Desert Rock, NV*	36.6	244.0	SURFRAD
Chesapeake Lighthouse, VA	36.9	284.3	LaRC
Boulder Tower, CO	40.1	255.0	GMD
Bondsville, IL	40.1	271.6	SURFRAD
Table Mountain, CO	40.1	254.8	SURFRAD
Penn State, PA	40.7	282.1	SURFRAD
Sioux Falls, SD	43.7	263.4	SURFRAD
Payerne, Switzerland	46.8	6.9	BSRN
Fort Peck, MT	48.3	254.9	SURFRAD
Lindenberg, Germany	52.2	14.1	BSRN
Barrow, AK	71.3	203.4	GMD
Ny Alesund, Norway	78.9	12.0	BSRN

where g_5 is a function of T_s and w, and ''C'' in the subscript signifies Model C. DLF for the cloudy part of the scene (F_{Ccld}) was derived as

$$F_{\mathrm{Ccld}} = g_6(T_s, w, \mathrm{lwp}, \mathrm{iwp}), \tag{10}$$

where g_6 is a function of the listed variables, and ''lwp'' and ''iwp'' are liquid water path and ice water path respectively for the cloud in the scene. For explicit forms of functions g_5 and g_6, the reader is referred to the previously cited references. All-sky DLF (F_{Call}) for the scene is then computed as

$$F_{\mathrm{Call}} = F_{\mathrm{Cclr}}(1 - A_c) + F_{\mathrm{Ccld}}A_c. \tag{11}$$

d. Model inputs

Meteorological inputs, namely, surface skin temperature, tropospheric temperature profile, and column water vapor, used by all three models were available from the MOA database, which is primarily based on the Goddard Earth Observing System 4 (GEOS-4) reanalysis product from the National Aeronautics and Space Administration (NASA) Global Modeling and Assimilation Office (GMAO; Bloom et al. 2005). Broadband and window surface emissivities used in Models A and B were adopted from the maps in Wilber et al. (1999). Cloud amounts used for computing all-sky fluxes in Models B and C, and lwp and iwp used in Model C, were all available internally from the CERES cloud subsystem (Minnis et al. 1997). Cloud-base temperature (T_{cb}) and column water vapor below cloud base (w_c) used in Model B [Eq. (8)] were computed by interpolating temperature and humidity profiles to the level of cloud-base pressure, which is also available from the cloud subsystem.

3. Flux overestimation: The problem

Comparisons of CERES single scanner footprint (SSF) fluxes derived with these models with ground-based measurements consistently showed that a significant number of points near the high end of the flux range were substantially overestimated (Kratz et al. 2010). Ground-based measurements were obtained from 30 sites around the globe belonging to either the Atmospheric Radiation Measurement Program (ARM), the National Oceanic and Atmospheric Administration (NOAA) Global Monitoring Division (GMD) network, which includes the U.S.-based Surface Radiation (SURFRAD) sites, or the international Baseline Surface Radiation Network (BSRN). Information regarding locations and affiliations of these sites is presented in Table 1. The authors obtained these data from the CERES/ARM Validation Experiment (CAVE) database (Rutan et al. 2001; data were obtained online at http://www-cave.larc.nasa.gov/cave/), which is maintained by the CERES Surface and Atmospheric Radiation Budget (SARB) working group for validation of CERES products and is available to the worldwide scientific community online (see http://www-cave.larc.nasa.gov/cave/). The top row in Fig. 1 shows comparisons with ground data for each model for clear-sky conditions, combined for all ground sites, based on 46 months (July 2002–April 2006) of CERES/*Aqua* edition-2B results (see Kratz et al. 2010). Each model shows similar overestimation at the high end of the flux range. A closer examination of the problem showed that overestimation was occurring more frequently at dry–arid sites. This is borne out clearly by corresponding scatterplots on the bottom row where points were included only from the six dry–arid sites identified in Table 1 by asterisks. Note that corresponding scatterplots for all-sky comparisons (not included here) show similar overestimation.

As discussed in section 2, all of the models make use of surface skin temperature (T_s) in the computation of the DLF either for estimating near-surface air temperature or as a substitute for this quantity. Even though a wide range

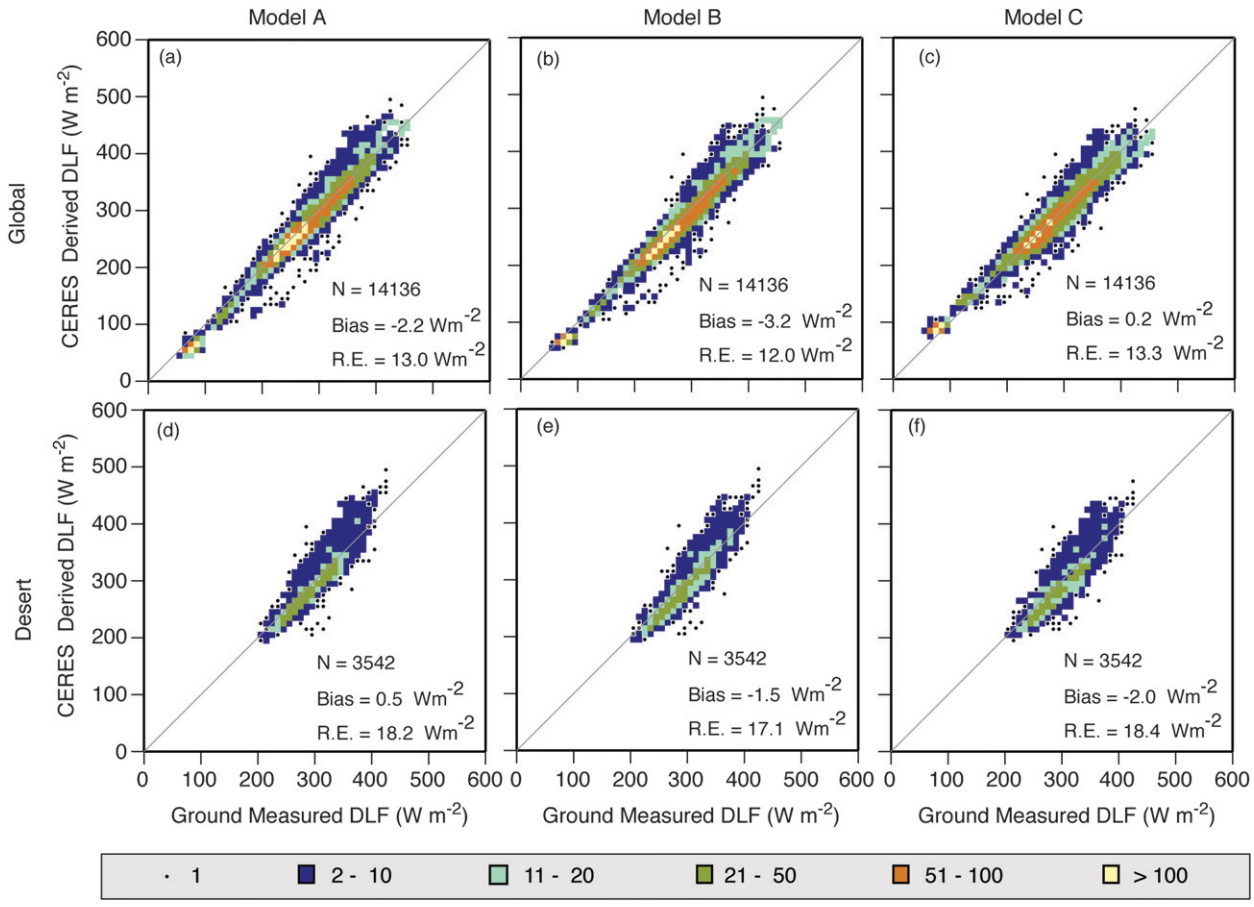

FIG. 1. Comparison of clear-sky fluxes derived with each model with ground-measured fluxes from the 30 sites listed in Table 1. (left) Model A and (middle) Model B fluxes were taken from CERES archive for 46 months (July 2002–April 2006). (right) Model C results were produced in an offline run using the same inputs. (top) Comparisons combined for all sites in Table 1. (bottom) The same for the six dry–arid sites identified in Table 1 by asterisks.

of meteorological datasets was used in the development of these models (see Gupta 1989), extremely high surface temperature conditions that result in lower tropospheric lapse rates that far exceed the dry adiabatic value ($\approx$10 K km^{-1}) occurred infrequently in those datasets The authors hypothesize that because of excessive daytime heating of the surface over dry–arid regions, especially during times of high surface insolation, effective lapse rates in the lower troposphere exceed that threshold resulting in an overestimation of DLF in these models. Even though the existence of overestimation problem was established in all three models, Model B was chosen for conducting detailed studies and for developing a solution with the expectation that the same or a similar solution could be applied to the other two models. In Model B, DLF is affected by high values of T_s through Eq. (6) where high values of T_s boost the values of T_e.

The use of T_s in the computation of DLF requires an explanation in view of the fact that, in a strict physical sense, downward flux should not be dependent on the skin temperature. The explanation lies in the weighting function of DLF reaching the surface shown in Fig. 2, derived with a radiative transfer model that uses an atmosphere stratified into 50-hPa layers (Gupta 1989). This weighting function derived for average midlatitude-type conditions shows that about 86% of the flux reaching the surface originates in the first 50-hPa layer and contributions from successive layers fall off rapidly. For warmer and more humid conditions, the contribution from the lowest layer would be expected to be even greater. Since this weighting function is peaked so close to the surface, correctly accounting for air temperature close to the surface is critical for realistic estimation of DLF. Reliable estimates of air temperature very close to the surface were not available in the pre-reanalysis era, and satellite-based sounders were widely used as sources of temperature and humidity profiles, especially for satellite-based algorithms of the type used in this work.

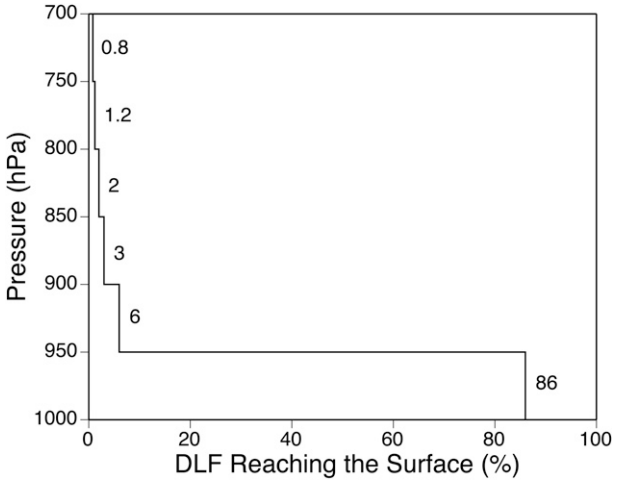

FIG. 2. Weighting function for DLF reaching the surface (midlatitude atmosphere; 50-hPa layers).

Since surface skin temperature was widely available from satellite-based sounders, it was readily used in such algorithms. The considerations outlined above provide the justification for using T_s in the computation of DLF, albeit as a proxy for air temperature very near the surface, for all models used in the present work and historically in most of the bulk formulas used in the past (Fung et al. 1984).

The primary reason for choosing Model B was the availability of a stand-alone version of this model that can be altered in ways required for the study and can be run as needed without interference with normal CERES processing. The stand-alone version is also used for another project, namely, the NASA Global Energy and Water Cycle Experiment (GEWEX) Surface Radiation Budget (SRB) project (hereinafter GEWEX/SRB; Stackhouse et al. 2004). The use of this version opens up opportunities for extensive validation of the model using a vast database of ground-based measurements developed under GEWEX/SRB. Results from operational CERES code, an offline version of CERES code used for testing proposed changes, as well as this stand-alone version will be used as appropriate throughout this work. The stand-alone version runs with inputs from the same GEOS-4 dataset, though those fields were regridded to a 1° longitude × 1° latitude global grid and temporally interpolated to 3-hourly to meet the requirements of the GEWEX/SRB project. Note that the resolution of original GEOS-4 data was 1.25° longitude × 1.00° latitude spatially and 6-hourly for temperature and humidity profiles and 3-hourly for surface parameters temporally. Cloud parameters used with the stand-alone version were derived in a 1° × 1° global grid from International Satellite Cloud Climatology Project (ISCCP; Rossow and Schiffer 1999) pixel-level (DX) data.

The stand-alone version was run globally for the year 2004 and results were compared with corresponding ground-based measurements from several BSRN sites. As expected, model results from certain sites showed significant overestimation near the high end of flux range. One such site, Alice Springs, Australia (23.8°S–133.9°E) located in a desert-like region was chosen as the focus of detailed studies as a representative of dry/arid regions. Analogous results from the Tateno, Japan (36.1°N–140.1°E), site were used as a control case representing a moderate climate region where no significant overestimation was observed.

Figure 3a shows the comparison of model-derived fluxes with ground-measured values for the Alice Springs site. These results show a large positive bias (20.9 W m^{-2}) coming mostly from points at the high end of the range. By comparison, bias in Tateno results (not shown) is only 1.5 W m^{-2}. As further tests of the above hypothesis, data from the Alice Springs comparison were separated between day and night and by the season. Figures 3b and 3c present scatterplots of data separated by day and night respectively and show that bias during daytime is much larger than during nighttime. The same data were also separated between four seasons: December–February (DJF), March–May (MAM), June–August (JJA), and September–November (SON). Scatterplots for DJF (summer in Southern Hemisphere) and JJA (winter) presented in Figs. 3d and 3e respectively show a much larger bias for DJF than for JJA. All of the above results strongly support the hypothesis that overestimation of the DLF is being caused by excessive heating of the surface during times of high surface insolation.

4. Flux overestimation: The solution

The relationship between severe overestimation of DLF and values of T_s was examined by getting an estimate of the lapse rate in the first model layer (surface–800 hPa) from the meteorological inputs for cases of severe overestimation. Model flux exceeding a corresponding ground measurement by 100 W m^{-2} was somewhat arbitrarily adopted as the threshold for severe overestimation. For the Alice Springs site, from 2490 3-hourly values that were matched with corresponding ground measurements over the entire year, 78 cases were found where overestimates exceeded the threshold of 100 W m^{-2}. Parameters related to these 78 cases relevant to the discussion of overestimation are presented in Table 2. Surface pressure (P_s) for these cases has a mean value of 940 hPa with a small range while T_s has a mean value of 325.5 K but a large range. The key parameter, however, is the temperature difference ($T_s - T_{800}$), which acts as an indicator of the first-layer lapse rate and has a mean value of 32.8 K with a large range.

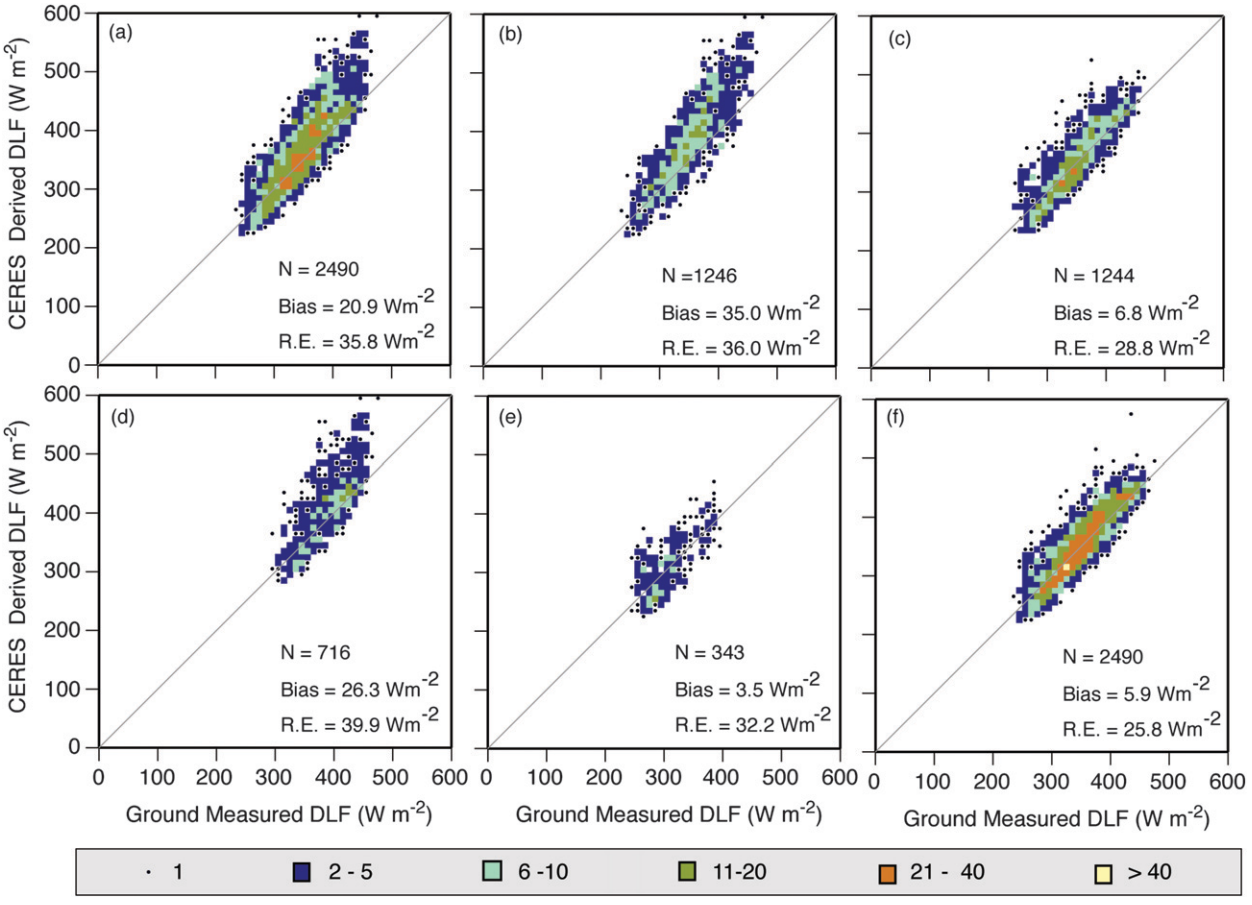

FIG. 3. Comparison of 3-hourly all-sky fluxes derived with the stand-alone version of Model B for all months of 2004 with ground-measured fluxes for the Alice Springs site for (a) all points, (b) daytime points, (c) nighttime points, (d) points for DJF season, and (e) points for JJA season. (f) Comparison for all points after applying the temperature constrainment technique.

Though this temperature difference is large, a direct comparison of this mean value with the nominal lapse rate of 6.5 K km^{-1} was difficult because temperature profiles in the input data are available in pressure coordinates only. The hypsometric equation [Wallace and Hobbs 2006, their Eq. (2.25)] was, therefore, used to convert profiles in pressure coordinates to those in geometrical ones. An examination of layer thicknesses using the hypsometric equation showed that geometrical thickness of a 100-hPa layer in the lower troposphere (1000–600 hPa) varies from 0.80 to 1.26 km over the globe. The highest among these values occurred in the tropics and at higher altitudes (between 700 and 600 hPa), and the lowest near the poles and close to the surface. Based on this examination, a 100-hPa pressure difference can be adopted as an approximate equivalent of 1 km in altitude and the 800-hPa level would be ≈1.5 km above the surface. Using a nominal lapse rate of about 6.5 K km^{-1}, $T_s - T_{800}$ should be ≈10 K under normal conditions, and should not exceed 15 K even when conditions of dry adiabatic lapse rate (≈10 K km^{-1}) exist. Note that 47 of the 78 cases of severe overestimation discussed above occurred in the DJF season while only one case occurred in the JJA season.

Based on the above analysis, an average first-layer lapse rate [K (100 hPa)$^{-1}$] was computed as $(T_s - T_{800})/(P_s - 800)$, and a value of 10 K (100 hPa)$^{-1}$ was adopted as an acceptable upper limit for the lower troposphere. A value exceeding this limit was taken as an indication of excessive heating of the surface. The value of T_s for such cases was constrained so as not to exceed

TABLE 2. Mean and range of various parameters for the 78 cases for which overestimation >100 W m^{-2}.

Parameter	Mean	Range
DLF overestimate (W m^{-2})	117	100–177
T_s (K)	325.5	290.6–337.2
T_{800} (K)	292.7	275.8–299.9
$T_s - T_{800}$ (K)	32.8	8.6–42.2
P_s (hPa)	940	932–947

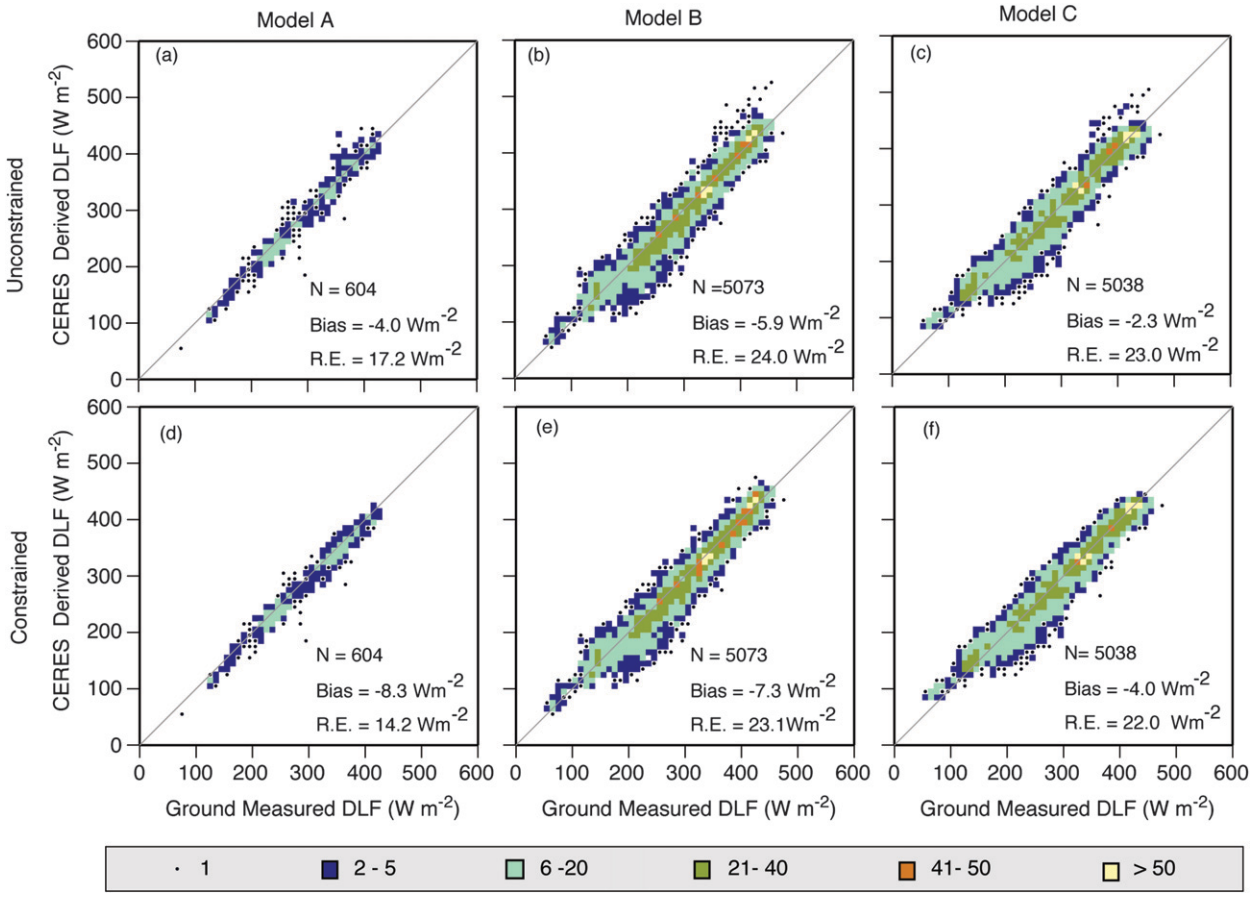

FIG. 4. Comparison of fluxes derived with each model with ground-measured fluxes from all sites in Table 1 (top) before and (bottom) after applying the constrainment technique. (left) Model A results are for clear sky only while those for Models (middle) B and (right) C are for all-sky conditions. Model results were produced with an offline version of CERES code run for January and July 2004.

this limit to get an appropriate value for use in Eq. (6), and subsequent computation of DLF. This constraint was implemented in the Model B code by computing the lapse rate in the first layer and adjusting T_s downward until the 10 K (100 hPa)$^{-1}$ restriction was met. The constrained surface temperature was denoted as T_{sc}. Note that an appropriately lower pressure level (instead of 800 hPa) was chosen for computing the lapse rate for regions where surface pressure was substantially lower than 1000 hPa. The same method was also used in Model A and Model C codes for computing T_{sc} that was subsequently used in computations of DLF with those codes. Note that unlike the DLF, the upward longwave flux for all models was still computed with the unconstrained value of T_s.

5. Results and discussion

Figure 3f shows results of the implementation of the constrainment technique in the stand-alone version of Model B for the Alice Springs site with the same inputs and for the same period as in Fig. 3a. Mean bias for the Alice Springs site is now reduced from 20.9 to 5.9 W m^{-2}. In contrast, the mean bias for the Tateno site (not shown) remained essentially unchanged. The constrainment technique was then implemented in the offline version of CERES code that was run with both *Terra* and *Aqua* inputs for January and July 2004. Results for the same two months were also extracted from operational CERES processing where the models were run without the constrainment technique. Figure 4 shows comparisons of unconstrained (top panels) and constrained (bottom panels) fluxes for the above two months with ground-based measurement from the same set of sites as used in Fig. 1. As expected, model-derived fluxes decreased as a result of constrainment for all models even though that caused larger negative biases in the new results. Despite this, the random error (R. E.), root-mean-square of residuals around the line of fit, decreased indicating a closer comparison between CERES-derived and ground-measured fluxes.

Since stand-alone model results are truly global and cover a continuous 12-month period, those were used to

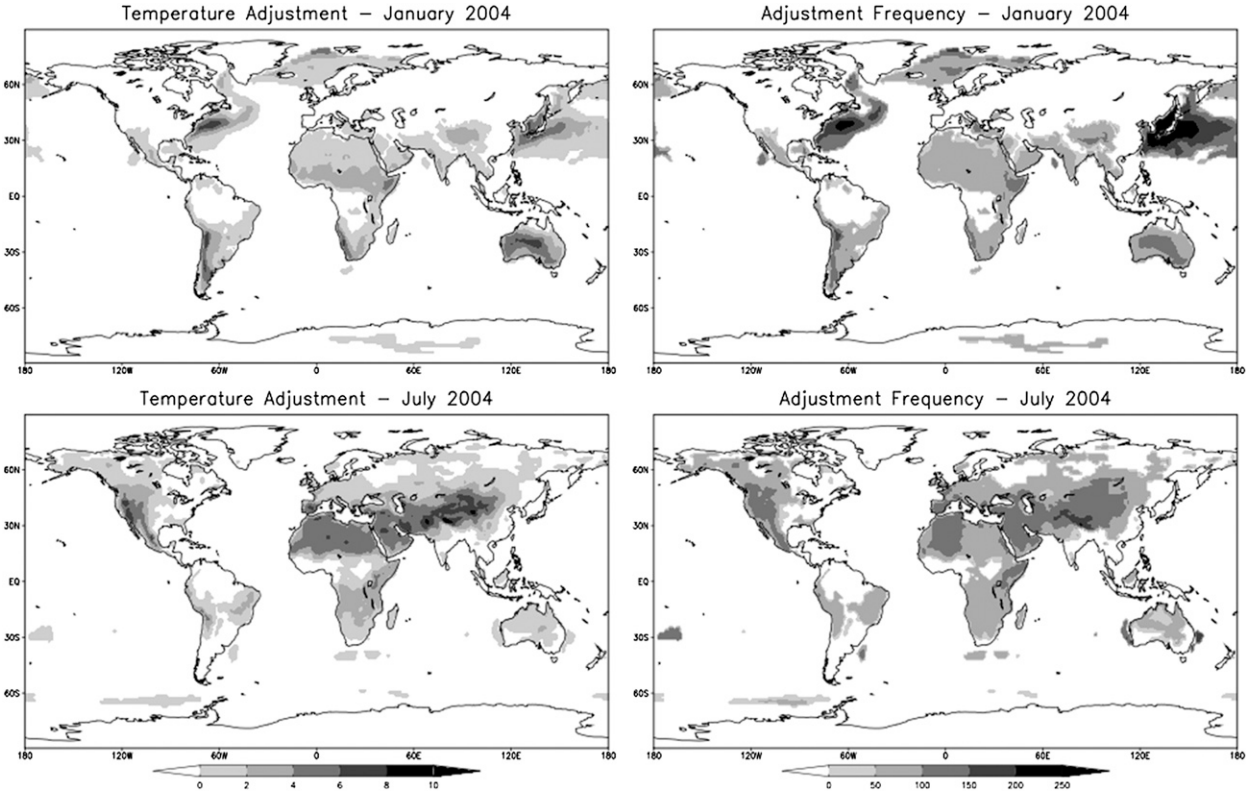

FIG. 5. Monthly average value of (left) temperature adjustment (K) and (right) frequency of temperature adjustment applied during the constrainment process for (top) January and (bottom) July 2004.

determine locations, magnitudes, and frequencies of temperature adjustments that were occurring as a result of the constrainment process. Figure 5 shows the geographical distribution of temperature adjustment (unconstrained–constrained) on a monthly average basis for January and July 2004 (left panels). The right panels in Fig. 5 show the frequency of occurrence of temperature adjustment (out of 248) for the two months. Note that the averages shown in the left panels are means of 248 (31 days $\times$ 8 times day^{-1}) values, and frequently, very small values occur among them when even a single nonzero adjustment occurs during the course of the whole month. Adopting values of zero for the magnitude as well as the frequency for those grid boxes where monthly average adjustment was <0.5 K eliminated those very small values. Such low values were taken as an indication of small magnitude and/or low frequency of occurrence of temperature adjustments.

The plots in Fig. 5 clearly show that larger magnitudes and higher frequencies of adjustments occur mostly over dry–arid land areas in the summer hemisphere where, as expected, excessive heating of the surface takes place at times of high surface insolation. A few ocean areas where this occurs are located off the east coasts of large continents in the winter hemisphere where cold westerly winds from the continents blow over relatively warmer ocean waters. Prime examples of these are the Sea of Japan and areas of Pacific Ocean to the east of Japan where cold westerly winds from the Asian mainland blow over warm waters of the Kuroshio, and areas off the east coast of North America where westerly winds blow over waters affected by the Gulf Stream. The relationship between T_s and air temperature aloft at 950

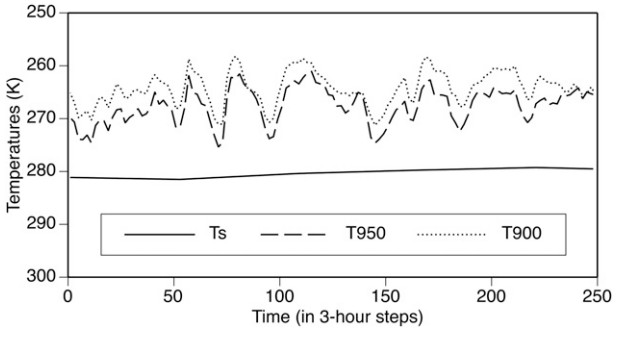

FIG. 6. Time series of surface skin temperature and temperatures at 950- and 900-hPa levels for a grid box over the Sea of Japan for January 2004.

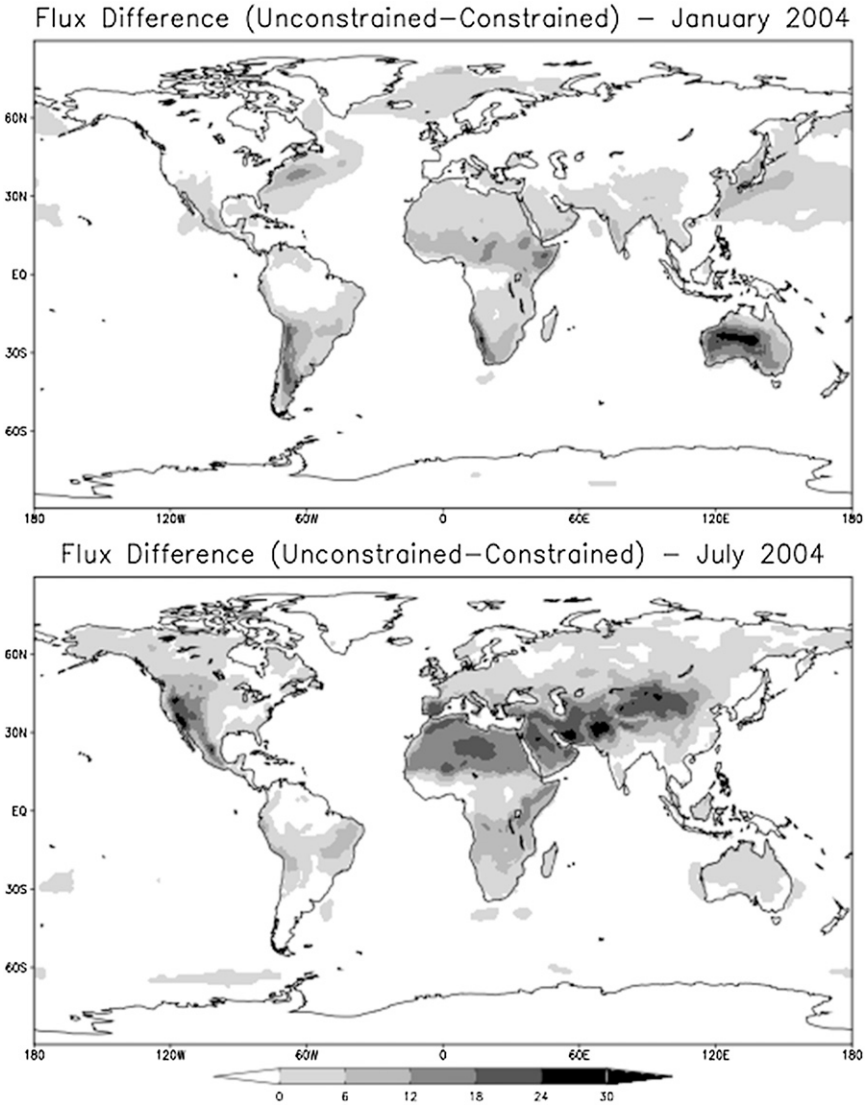

FIG. 7. Monthly average difference between unconstrained and constrained fluxes (W m^{-2}) for (top) January and (bottom) July 2004. This difference (unconstrained − constrained) represents the adjustment applied to the unconstrained fluxes to remedy the overestimation.

and 900 hPa (T_{950} and T_{900} respectively) over the Sea of Japan was examined to assess the magnitude of adjustment for such areas. Figure 6 shows 3-hourly time series of T_s, T_{950}, and T_{900} for a 1° × 1° grid box (40°–41°N, 135°–136°E) over the Sea of Japan during January 2004. These time series show T_s to be steady around 280 K but T_{950} and T_{900} to be highly variable and much lower than T_s. The difference ($T_s - T_{900}$), representing the lapse rate, was found to vary from 9 to 22 K with a monthly mean of 16 K while a value around 7 K would be expected under normal lapse rate conditions. The magnitude of the effect of temperature constrainment on surface fluxes is shown in Fig. 7 for the above two months on a monthly average basis. Note that this is the difference between unconstrained and constrained fluxes and, therefore, represents the overestimation that was occurring in the unconstrained computation. As expected, the geographical distribution of this difference closely follows that of the temperature adjustment shown in the left panels of Fig. 5. Here again, the very small values were eliminated from the graphic by adopting a zero value for those grid boxes where monthly average flux difference was <1.0 W m^{-2}.

6. Summary and concluding remarks

A methodology was developed and demonstrated for correcting the overestimation of DLF in the three LW algorithms used in the SOFA segment of the CERES

processing system for deriving surface LW fluxes. This overestimation was observed in instantaneous SSF fluxes, derived with all three models from both *Terra* and *Aqua* measurements, during validation against ground-measured fluxes over a period of 5–6 yr primarily over ground sites located in dry/arid areas. This overestimation was most conspicuous during summer months at the high end of the flux range. An examination of corresponding temperature profiles (from meteorological input data) showed that T_s in such profiles was much higher than air temperature at levels 100 and 200 hPa above the surface, resulting in a lapse rate in the lower troposphere that exceeded even the dry adiabatic value.

Flux overestimation was observed in results of all three models and Model B was chosen for use in a closer investigation. The ground site at Alice Springs, Australia, located in a desert-type region, was chosen as a representative of dry–arid areas. Comparison of model results with corresponding ground-based measurements showed significant overestimation mostly coming from the high end of the flux range. Most of the overestimation occurred during daytime and was most pronounced during the summer season. These observations strongly supported the hypothesis that overestimation occurred as a result of excessive heating of the surface during times of high surface insolation, a statement that turned out to be strictly true for land areas only. Over a few ocean areas, off the east coasts of large continents in the winter hemisphere, significant overestimation occurred but for a different reason. In these cases, the large temperature difference between the surface and the atmosphere was caused by cold westerly winds from the continents blowing over relatively warmer waters.

A two-step procedure was developed to remedy this overestimation based on an analysis of the Alice Springs comparisons. The first step was designed to detect meteorological conditions potentially leading to overestimation and the second step to apply an adjustment to T_s to limit the value of lower-tropospheric lapse rate. Application of this procedure for all months of 2004 and subsequent comparison with ground data at Alice Springs showed that the large positive bias seen earlier was greatly reduced. Overestimation was not occurring at the Tateno site and application of the adjustment procedure had no significant effect on fluxes. This work also addresses a persistent question regarding the use of T_s in the computation of DLF in these models because, in principle, DLF should not be dependent on T_s. The answer to this question was found to lie in the weighting function for DLF reaching the surface, which peaks very close to the surface. Under most atmospheric conditions, T_s is closely linked to the air temperature next to the surface and thus works well as a proxy for the air temperature.

Acknowledgments. ARM data have been made available through the U.S. Department of Energy as part of the Atmospheric Radiation Measurement Program. GMD data have been made available through NOAA's Earth System Research Laboratory/Global Monitoring Division–Radiation (G-RAD). SURFRAD data have been made available through NOAA's Air Resources Laboratory/Surface Radiation Research Branch. The authors thank D. A. Rutan (SSAI) for providing the CAVE database and E. G. Dutton for making available the BSRN data. The authors also thank G. Gibson (LaRC) for a critical review of the manuscript and suggesting many valuable improvements.

REFERENCES

Bloom, S., and Coauthors, 2005: Documentation and validation of the Goddard Earth Observing System (GEOS) Data Assimilation System – Version 4. NASA Tech. Memo. TM-2005-104606, Vol. 26, 187 pp.

Fung, I., D. E. Harrison, and A. A. Lacis, 1984: On the variability of the net longwave radiation at the ocean surface. *Rev. Geophys. Space Phys.,* **22,** 177–193.

Gupta, S. K., 1989: A parameterization for longwave surface radiation from Sun-synchronous satellite data. *J. Climate,* **2,** 305–320.

——, W. L. Darnell, and A. C. Wilber, 1992: A parameterization for longwave surface radiation from satellite data: Recent improvements. *J. Appl. Meteor.,* **31,** 1361–1367.

Inamdar, A. K., and V. Ramanathan, 1997: On monitoring the atmospheric greenhouse effect from space. *Tellus,* **49B,** 216–230.

Kratz, D. P., S. K. Gupta, A. C. Wilber, and V. E. Sothcott, 2010: Validation of the CERES edition 2B surface–only flux algorithms. *J. Appl. Meteor. Climatol.,* **49,** 164–180.

Loeb, N. G., S. Kato, K. Loukachine, and N. Manalo-Smith, 2005: Angular distribution models for top-of-atmosphere radiative flux estimation from the Clouds and the Earth's Radiant Energy System instrument on the *Terra* satellite. Part I: Methodology. *J. Atmos. Oceanic Technol.,* **22,** 338–351.

——, ——, ——, ——, and D. R. Doelling, 2007: Angular distribution models for top-of-atmosphere radiative flux estimation from the Clouds and the Earth's Radiant Energy System instrument on the *Terra* satellite. Part II: Validation. *J. Atmos. Oceanic Technol.,* **24,** 564–584.

Minnis, P., and Coauthors, 1997: Cloud Optical Property Retrieval (System 4.3). CERES Algorithm Theoretical Basis Doc., ATBD Release 2.2, NASA/RP-1376, 60 pp. [Available online at http://asd-www.larc.nasa.gov/ATBD/ATBD.html.]

Rossow, W. B., and R. A. Schiffer, 1999: Advances in understanding clouds from ISCCP. *Bull. Amer. Meteor. Soc.,* **80,** 2261–2287.

Rutan, D. A., F. G. Rose, N. M. Smith, and T. P. Charlock, 2001: Validation data set for CERES surface and atmospheric radiation budget (SARB). *GEWEX News,* **11,** No. 1, International GEWEX Project Office, Silver Spring, MD, 11-12.

Stackhouse, P. W., S. K. Gupta, S. J. Cox, J. C. Mikovitz, T. Zhang, and M. Chiacchio, 2004: 12-year surface radiation budget data set. *GEWEX News,* **14,** No. 4, International GEWEX Project Office, Silver Spring, MD, 10–12.

Stephens, G. L., and P. J. Webster, 1984: Cloud decoupling of surface and planetary radiative budgets. *J. Atmos. Sci.,* **41,** 681–686.

——, A. Slingo, M. J. Webb, P. J. Minnett, P. H. Daum, L. Kleinman, I. Wittmeyer, and D. A. Randall, 1994: Observations of the Earth's radiation budget in relation to atmospheric hydrology. 4. Atmospheric column radiative cooling over the world's oceans. *J. Geophys. Res.,* **99** (D9), 18 585–18 604.

Wallace, J. M., and P. V. Hobbs, 2006: *Atmospheric Science: An Introductory Survey*. Elsevier Science, 504 pp.

Wielicki, B. A., B. R. Barkstrom, E. F. Harrison, R. B. Lee III, G. L. Smith, and J. E. Cooper, 1996: Clouds and the Earth's Radiant Energy System (CERES): An Earth Observing System experiment. *Bull. Amer. Meteor. Soc.,* **77,** 853–868.

Wilber, A. C., D. P. Kratz, and S. K. Gupta, 1999: Surface emissivity maps for use in satellite retrievals of longwave radiation. NASA Tech. Publication TP-1999-209362, 35 pp.

Zhou, Y., and R. D. Cess, 2001: Algorithm development strategies for retrieving the downwelling longwave flux at the Earth's surface. *J. Geophys. Res.,* **106,** 12 477–12 488.

——, D. P. Kratz, A. C. Wilber, S. K. Gupta, and R. D. Cess, 2007: An improved algorithm for retrieving surface downwelling longwave radiation from satellite measurements. *J. Geophys. Res.,* **112,** D15102, doi:10.1029/2006JD008159.